Viscoelastic simulation of PET stretch/blow molding process

Fabrice Schmidt, Jean-François Agassant, Michel Bellet, Luc Desoutter

Viscoelastic simulation of PET stretch/blow molding process

F.M. Schmidt[a,*], J.F. Agassant[a], M. Bellet[a], L. Desoutter[b]

[a]*Ecole des mines de Paris, CEMEF-URA CNRS no. 1374, 06904 Sophia-Antipolis, France*
[b]*SIDEL Corporation, 76600 Le Havre, France*

Received 4 August 1995; in revised form 4 December 1995

Abstract

In the stretch/blow molding process of poly(ethylene terephthalate) (PET) bottles, various parameters such as displacement of the stretch rod, inflation pressure, and polymer temperature distribution, have to be adjusted in order to improve the process. An axisymmetric numerical simulation code has been developed using a volumic approach. The numerical model is based on an updated-Lagrangian finite element method together with a penalty treatment of mass conservation. An automatic remeshing technique has been used. In addition, a decoupled technique has been developed in order to compute the viscoelastic constitutive equation. Successful stretch/blow molding simulations have been performed and compared to experiments.

Keywords: Finite element method; Splitting technique; Stretch/blow molding; Viscoelastic fluid

1. Introduction

1.1. Description of the stretch/blow molding process

An amorphous injected molded tube-shaped preform of poly(ethylene terephthalate) (PET) is heated in an infrared oven above the glass transition temperature ($T \approx 100°C$), transferred inside a mold and then inflated with stretch rod assistance in order to obtain the desired bottle shape (Fig. 1). The performance of the produced bottle (wall thickness distribution, transparency, mechanical properties . . .) is determined both by the material properties and the operating conditions: the initial preform shape, the initial preform temperature and the balance between stretching and blowing rate.

*Corresponding author.

1.2. *Literature on blow molding simulations*

Numerical simulations of the blow or stretch/blow molding processes have been extensively developed during the last decade. Most of the models assume a thin shell description of the parison. Warby and Whiteman [1] as well as De Lorenzi and coworkers [2,3] propose isothermal finite element calculations. These models, first developed for thermoforming processes, have since been applied to the blow molding process. The rheological behavior is given by a nonlinear-elastic constitutive equation derived from the rubber-like theory. Kouba and Vlachopoulos [4] have extended the previous model to the blow molding of a viscoelastic fluid (KBKZ constitutive equation). Several models use a volumic finite element approach. In 1986, Cesar de Sa [5] simulated the blowing process of glass parisons assuming Arrhenius temperature dependent Newtonian behavior. Chung [6] has carried out simulations of PET stretch/blow molding using the code ABAQUS®. The model assumes elasto-visco-plastic behavior and thermal effects are neglected. Poslinski and Tsamopoulos [7] have introduced nonisothermal parison inflation in a simplified geometry. In order to take into account the phase change, the latent heat of solidification has been included in the heat capacity of the material. Recently, Debbaut et al. [8] have also performed viscoelastic blow molding simulations with a Giesekus constitutive equation. They introduce thermal effects but present numerical results only in the case of a Newtonian fluid.

In blow molding simulations, numerical models have to take into account large biaxial deformations of the material, the evolving contact between tools (mold and stretch rod) and polymer, and temperature gradients. In the stretch/blow molding process, the contact between the stretch rod and the bottom of the preform induces localized deformations which need volumic approaches in order to obtain an accurate description.

1.3. *Objectives of the present approach*

In a previous paper [9], we pointed out that the computed stretching force using a Newtonian volumic model was very far from the experimental one. In the present work, an isothermal

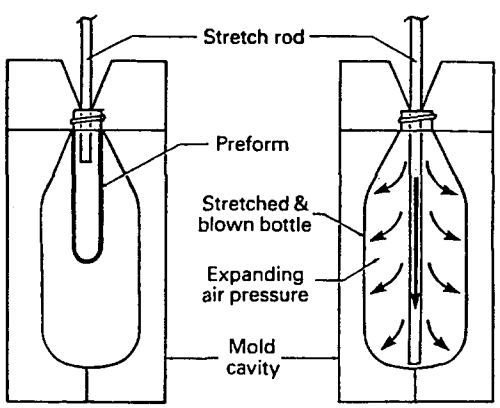

Fig. 1. Description of the stretch/blow molding step.

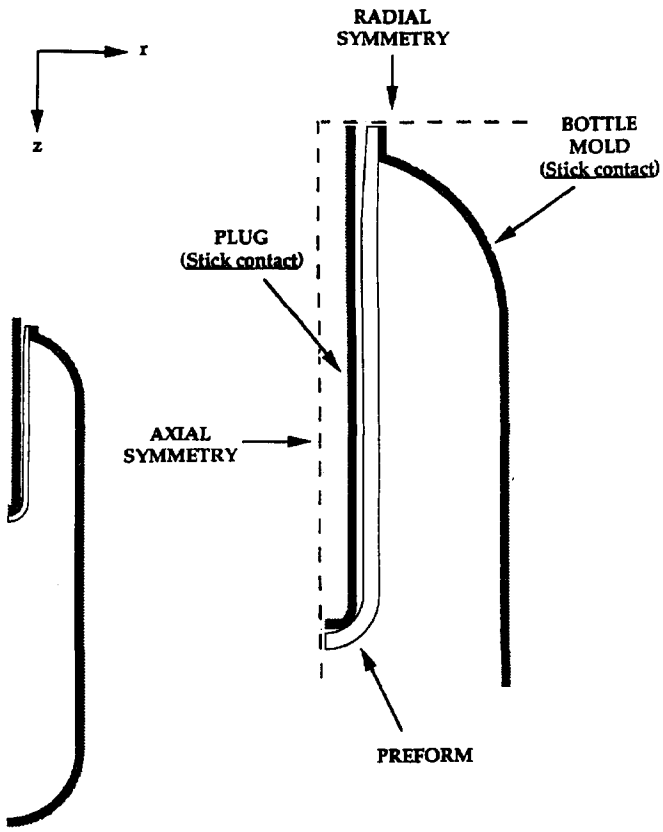

Fig. 2. Boundary conditions.

finite element volumic calculation of the PET stretch/blow molding of a viscoelastic fluid is presented. The improvement in terms of force prediction will be shown. Thickness and stress profiles in the bottle will be discussed.

2. Basic equations and boundary conditions

The material is assumed to be incompressible, so, the continuity equation may be expressed as

$$\nabla \cdot \vec{u} = 0 \quad \text{on } \Omega, \tag{1}$$

where $\vec{u}$ is the velocity field and Ω is the domain occupied by the parison. In addition, the weak form of the dynamic equilibrium can be written over the whole domain Ω at any time t and for any velocity field $\vec{u}^*$:

$$\int_\Omega \boldsymbol{\sigma} : \dot{\boldsymbol{\epsilon}}^* \, dv + \int_\Omega \rho \vec{\gamma} \cdot \vec{u}^* \, dv = \int_\Gamma (\boldsymbol{\sigma} \cdot \vec{n}) \cdot \vec{u}^* \, dS + \int_\Omega \rho \vec{g} \cdot \vec{u}^* \, dv. \tag{2}$$

$\boldsymbol{\sigma}$ is the Cauchy stress tensor; ρ, the specific mass; $\vec{\gamma}$, the acceleration; $\vec{g}$, the acceleration due to gravity; $\dot{\boldsymbol{\epsilon}}^* = \frac{1}{2}(\nabla\vec{u}^* + {}^{\mathrm{T}}\nabla\vec{u}^*)$, the rate of strain tensor associated with $\vec{u}^*$; $\vec{n}$, the unit outward normal vector to the boundary of the domain Γ.

In the present approach, the liquid-like viscoelastic constitutive equation of Johnson–Segalman type [10] with additional solvent viscosity is used:

$$\boldsymbol{\sigma} = -p'\boldsymbol{I} + 2\eta_s\dot{\boldsymbol{\epsilon}} + \boldsymbol{T} \quad \text{on } \Omega, \tag{3}$$

where p' is an arbitrary pressure; $\boldsymbol{I}$, the identity tensor; $\boldsymbol{T}$, the extra-stress tensor which is related to $\dot{\boldsymbol{\epsilon}}$ by a nonlinear partial differential equation:

$$\boldsymbol{T} + \lambda\frac{\mathrm{D}\boldsymbol{T}}{\mathrm{D}t} = 2\eta_v\dot{\boldsymbol{\varepsilon}}. \tag{4}$$

λ is the relaxation time; η_s and η_v are the viscous part and the viscoelastic part respectively of the total viscosity η ($\eta = \eta_s + \eta_v$). η and λ are constant in the case of an isothermal computation. For the stability of the simulations, we took $\eta_s > \eta_v/8$ according to the criteria of Crochet et al. [11]. D/Dt is the Gordon–Schowalter convective time derivative:

$$\frac{\mathrm{D}\boldsymbol{T}}{\mathrm{D}t} = \frac{\partial\boldsymbol{T}}{\partial t} + (\vec{u}\cdot\nabla)\boldsymbol{T} + \boldsymbol{T}\cdot\boldsymbol{\Omega} - \boldsymbol{\Omega}\cdot\boldsymbol{T} - a(\dot{\boldsymbol{\varepsilon}}\cdot\boldsymbol{T} + \boldsymbol{T}\cdot\dot{\boldsymbol{\varepsilon}}), \tag{5}$$

where $\boldsymbol{\Omega} = \frac{1}{2}(\nabla\vec{u} - {}^{\mathrm{T}}\nabla\vec{u})$ is the rotation tensor; $a \in [-1, +1]$ is the "slip" parameter which determines the type of convective derivative. For $a = 1$ (upper-convected), we recover the Oldroyd B model.

The initial geometry of the preform and the boundary conditions are presented in Fig. 2. The boundary Γ of the domain Ω is decomposed as

$$\Gamma = \Gamma^{\mathrm{v}} \cup \Gamma^{\mathrm{p}} \cup \Gamma^{\mathrm{f}}, \tag{6}$$

where Γ^{v} is the part of the boundary Γ where the velocity is prescribed (bottom of the rod), Γ^{p} the part of the boundary Γ where a pressure is applied and Γ^{f} the part of the boundary Γ contacting the tools.

External free surface $\Gamma^{\mathrm{p}}_{\mathrm{ext}}$. A zero pressure condition is assumed, serving as a reference for pressure values (this could just as well be the atmospheric pressure or even an evolving pressure resulting from the balance between air compression between the preform and the mold and air leakage flow through the vents of the mold, but this will not be considered here):

$$\boldsymbol{\sigma}\cdot\vec{n} = \vec{0}. \tag{7}$$

Internal free surface $\Gamma^{\mathrm{p}}_{\mathrm{int}}$. A differential inflation pressure $\Delta P(t)$ is applied which can evolve during the successive blowing stages:

$$\boldsymbol{\sigma}\cdot\vec{n} = -\Delta P\cdot\vec{n}. \tag{8}$$

Regions in contact with the tools Γ^f. A Newtonian friction law is assumed, which can be defined as

$$(\boldsymbol{\sigma} \cdot \vec{n})\vec{t} = -\alpha_f \eta \Delta \vec{u}\vec{t}, \tag{9}$$

where α_f is the friction coefficient ($\alpha_f = 0$ results in a perfectly sliding contact); $\vec{t}$, the unit tangential vector; $\Delta\vec{u}$, the velocity difference along the tools interface. A perfectly sticking contact can also be considered, assuming that any contacting node remains fixed until the end of the process. In addition, the non-penetration condition is written

$$\Delta\vec{u} \cdot \vec{n} \leq 0. \tag{10}$$

Regions where the velocity of the nodes is prescribed Γ^v.

$$\vec{u} \cdot \vec{n} = \vec{u}_{\text{tools}} \cdot \vec{n}. \tag{11}$$

3. Numerical resolution

3.1. Explicit time-marching algorithm

The whole process is divided into time intervals Δt_i so that the current time t_n may be written

$$t_n = \sum_{i=1}^{n} \Delta t_i \qquad (n \geq 1). \tag{12}$$

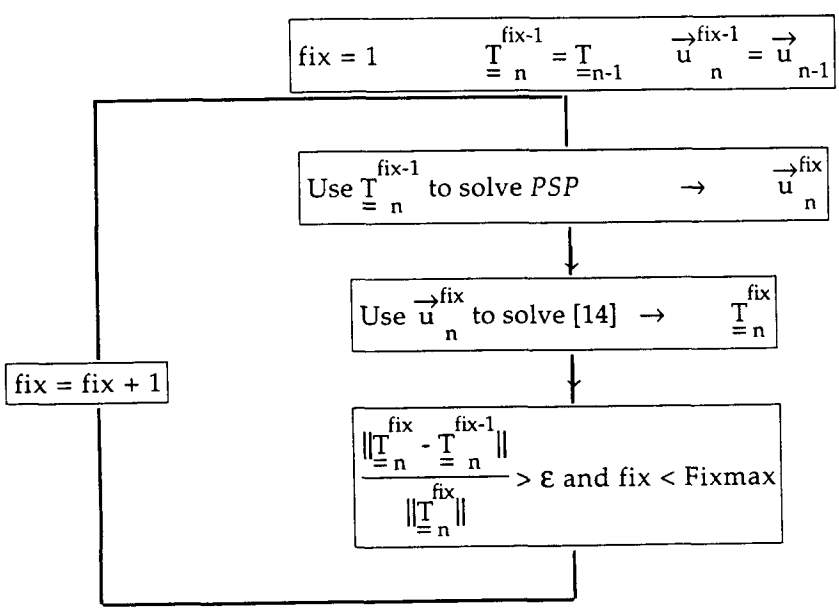

Fig. 3. Fixed-point algorithm.

At each time step t_n, the mechanical equations (see Sections 3.2 and 3.3) are solved on the deformed configuration Ω_n; the current values of the velocity vector $\vec{u}_n$, the pressure p'_n, and the extra-stress tensor $\boldsymbol{T}_n$ are computed. In order to compute the acceleration field $\vec{\gamma}_n$, we use a Newmark type [12] integration rule:

$$\vec{\gamma}_n = \frac{1}{\theta}\left(\frac{\vec{u}_n - \vec{u}_{n-1}}{\Delta t_n} - (1-\theta)\cdot\vec{\gamma}_{n-1}\right), \tag{13}$$

where θ is the arbitrary implicit parameter, which belongs to [0,1].

Then, the geometry is updated from Ω_n to Ω_{n+1} using the second order explicit Euler rule:

$$\vec{X}_{n+1} = \vec{X}_n + \Delta t_{n+1}\cdot\vec{u}_n + \frac{\Delta t_{n+1}^2}{2}\cdot\vec{\gamma}_n, \tag{14}$$

where $\vec{X}_n$ is the coordinate vector at time t_n.

3.2. Time descretization of the constitutive equation

The time differential constitutive equation (4) is approximated by an implicit Euler's scheme over the time increment Δt_n. This fully-implicit algorithm leads to

$$\boldsymbol{T}_n + \lambda\left[\frac{\boldsymbol{T}_n - \boldsymbol{T}_{n-1}}{\Delta t_n} + \boldsymbol{T}_n\cdot\boldsymbol{\Omega}_n - \boldsymbol{\Omega}_n\cdot\boldsymbol{T}_n - a(\dot{\boldsymbol{\epsilon}}_n\cdot\boldsymbol{T}_n + \boldsymbol{T}_n\cdot\dot{\boldsymbol{\epsilon}}_n)\right] = 2\eta_v\dot{\boldsymbol{\varepsilon}}_n, \tag{15}$$

where $\boldsymbol{T}_{n-1}$ has been calculated on the domain Ω_{n-1} at the previous time step. Such an implicit algorithm is well known for its non-conditional stability.

3.3. Splitting technique

Using Eqs. (3) and (5) and the boundary conditions (7)–(11), Eq. (2) can be written at each time t_n:

$$\int_{\Omega_n} 2\eta_s\dot{\boldsymbol{\epsilon}}_n:\dot{\boldsymbol{\epsilon}}^*\,\mathrm{d}v - \int_{\Omega_n} p'_n\nabla\cdot\vec{u}^*\,\mathrm{d}v + \int_{\Omega_n}\boldsymbol{T}_n:\dot{\varepsilon}^*\,\mathrm{d}v + \int_{\Gamma_n^p}\Delta P\cdot\vec{n}\vec{u}^*\,\mathrm{d}S$$
$$+ \int_{\Gamma_n^f}\alpha_f\eta(\Delta\vec{u}\vec{t})\cdot\vec{t}\vec{u}^*\,\mathrm{d}S + \int_{\Omega_n}\rho(\vec{\gamma}_n - \vec{g})\cdot\vec{u}^*\,\mathrm{d}v = 0. \tag{16}$$

In order to solve Eqs. (15) and (16) together with the incompressibility condition (1), two families of computation methods are available: the coupled methods which solve the complete discretized equations and the decoupled methods, which split the global set of equations into two sub-systems, which are successively solved. For a complete review of these techniques, see Keunings [13], Basombrio [14] and Baaijens [15].

In this paper, a splitting technique is presented. At each time step, an iterative procedure based on a fixed-point method is used. The first sub-problem, called the Perturbed Stokes Problem (PSP), deals with an incompressible Newtonian fluid flow, perturbed by a known extra-stress tensor computed at the previous fixed-point iteration (fix-1). The second sub-

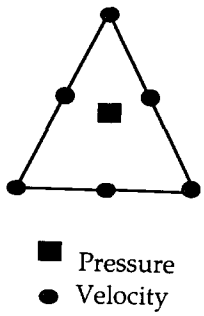

Fig. 4. P2-P0 element.

problem consists in determining the components of the extra-stress tensor for a known velocity vector by solving the time-discretized constitutive equation (15). The procedure is repeated until convergence. This algorithm is enforced by a dichotomic procedure on the time step in the case of non-convergence of the algorithm after a few iterations (Fixmax ≈ 10). For each time step t_n, the complete procedure is summarized in Fig. 3.

3.4. Numerical resolution of the viscoelastic equation

As the different integrals in Eq. (15) are evaluated by the Gauss–Legendre point integration rule, the components of the current extra-stress tensor $\boldsymbol{T}_n$ are only needed at the Gaussian points of each element. Consequently, the tensorial equation (15) is solved at a local level; it reduces to a (4×4) linear algebraic system.

3.5. Finite element approximation for PSP

The reference domain Ω_n is approximated by a set of 6-node isoparametric triangles (P2 element). Each point $\vec{X}_n$ of the elementary domain Ω_n^e is located by means of the vector of nodal position $\vec{X}_n^e$ and the matrix $\boldsymbol{N}$ of shape functions

$$\vec{X}_n = \boldsymbol{N}\vec{X}_n^e. \tag{17}$$

The current value of the velocity field $\vec{u}_n$ is expressed in terms of the nodal velocity vectors $\vec{u}_n^e$ with the same shape functions:

$$\vec{u}_n = \boldsymbol{N}\vec{u}_n^e. \tag{18}$$

The incompressibility constraint (1) is prescribed in a penalized form as

$$\nabla \cdot \vec{u}_n = -\frac{p'_n}{\rho_p}. \tag{19}$$

in which, ρ_p the penalty coefficient, is a large number (typical value is 10^7). It is to be noted that the penalty method is equivalent to the resolution using a discontinuous pressure, constant per element (see Fig. 4).

For the virtual velocity $\vec{u}^*$, we use the same approximation as for the velocity field (Galerkin method). Thus, the momentum equation (16) becomes

$$\boldsymbol{C} \cdot \vec{V} = \vec{F}, \tag{20}$$

where the vector $\vec{V}$ is the assembly of the nodal velocity components:

$$\vec{V} = \sum_{e=1}^{N_e} \vec{u}_n^e. \tag{21}$$

$\vec{F}$ is the vector of the applied forces:

$$\vec{F} = \sum_{e=1}^{N_e} (\vec{F}_\rho^e + \vec{F}_T^e + \vec{F}_g^e) + \sum_{b=1}^{N_b} (\vec{F}_p^b + \vec{F}_f^b). \tag{22}$$

The inertia forces $\vec{F}_\rho^e$ are given by

$$\vec{F}_\rho^e = \frac{\rho}{\theta}\left[\frac{\vec{u}_{n-1}^e}{\Delta t_n} + (1-\theta)\cdot \vec{\gamma}_{n-1}^e\right] \int_{\Omega_n^e} {}^T\boldsymbol{N} \cdot \boldsymbol{N}\, \mathrm{d}v^e. \tag{23}$$

The viscoelastic forces $\vec{F}_T^e$ which come from the 4-component extra-stress vector $\vec{T}_n$ at current time t_n are set by

$$\vec{F}_T^e = -\int_{\Omega_n^e} \vec{T}_n \cdot \mathrm{D}\boldsymbol{N}\, \mathrm{d}v^e. \tag{24}$$

The gravity forces are expressed by

$$\vec{F}_g^e = \rho \vec{g} \int_{\Omega_n^e} \boldsymbol{N}\, \mathrm{d}v^e. \tag{25}$$

The forces associated with the application of inflation pressure are

$$\vec{F}_p^b = -\int_{\Gamma_n^b} \Delta P \vec{n} \cdot \boldsymbol{N}\, \mathrm{d}S^b. \tag{26}$$

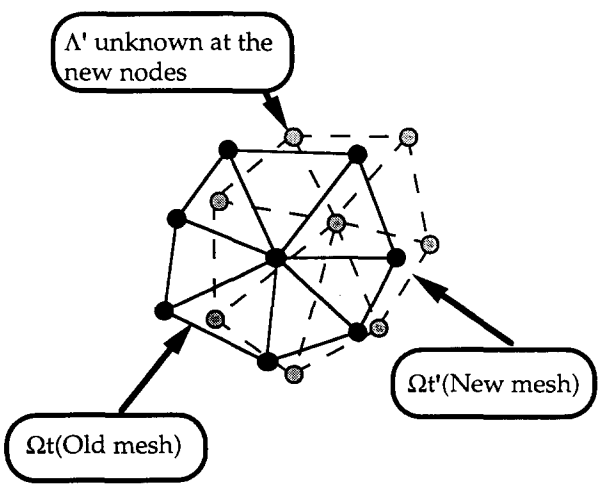

Fig. 5. Position of the nodes after remeshing.

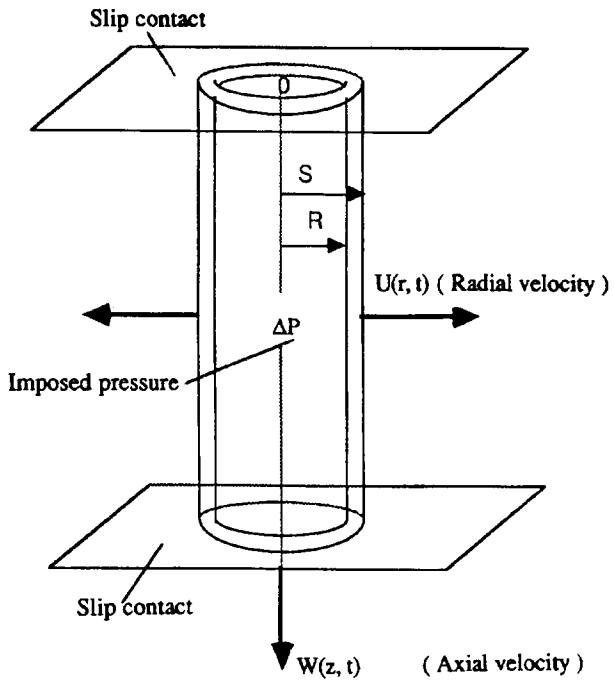

Fig. 6. Simultaneous inflation and extension of a tube.

The friction forces are

$$\vec{F}_{\mathrm{f}}^{\mathrm{b}} = -\int_{\Gamma_n^b} \alpha_{\mathrm{f}} \eta_{\mathrm{s}} \Delta \vec{u}_{\mathrm{t}} \cdot \boldsymbol{N}\, \mathrm{d}S^b. \tag{27}$$

$\boldsymbol{C}$ is the matrix defined by

$$\boldsymbol{C} = \sum_{e=1}^{N_{\mathrm{e}}} (\boldsymbol{C}_{\rho}^{\mathrm{e}} + \boldsymbol{C}_{\rho_{\mathrm{p}}}^{\mathrm{e}} + \boldsymbol{C}_{\eta_{\mathrm{s}}}^{\mathrm{e}}). \tag{28}$$

The elementary mass matrix $\boldsymbol{C}_{\rho}^{\mathrm{e}}$ is

$$\boldsymbol{C}_{\rho}^{\mathrm{e}} = \frac{\rho}{\theta \Delta t_n} \int_{\Omega_n^{\mathrm{e}}} {}^{\mathrm{T}}\boldsymbol{N} \cdot \boldsymbol{N}\, \mathrm{d}v^{\mathrm{e}}. \tag{29}$$

$\boldsymbol{C}_{\rho_{\mathrm{p}}}^{\mathrm{e}}$ corresponds to the incompressibility requirement:

$$\boldsymbol{C}_{\rho_{\mathrm{p}}}^{\mathrm{e}} = \rho_{\mathrm{p}} \int_{\Omega_n^{\mathrm{e}}} {}^{\mathrm{T}}\boldsymbol{\nabla} \cdot \boldsymbol{N} \cdot (\boldsymbol{\nabla} \cdot \boldsymbol{N})\, \mathrm{d}v^{\mathrm{e}}. \tag{30}$$

Table 1
Physical data and process parameters

S_0 (m)	R_0 (m)	L_0 (m)	v_0 (m s^{-1})	ΔP (Pa)	ρ (kg m^{-3})	λ (s)	η_{v} (Pa · s)
0.13	0.09275	0.125	0.4	10^6	1380	0.1	2.10×10^5

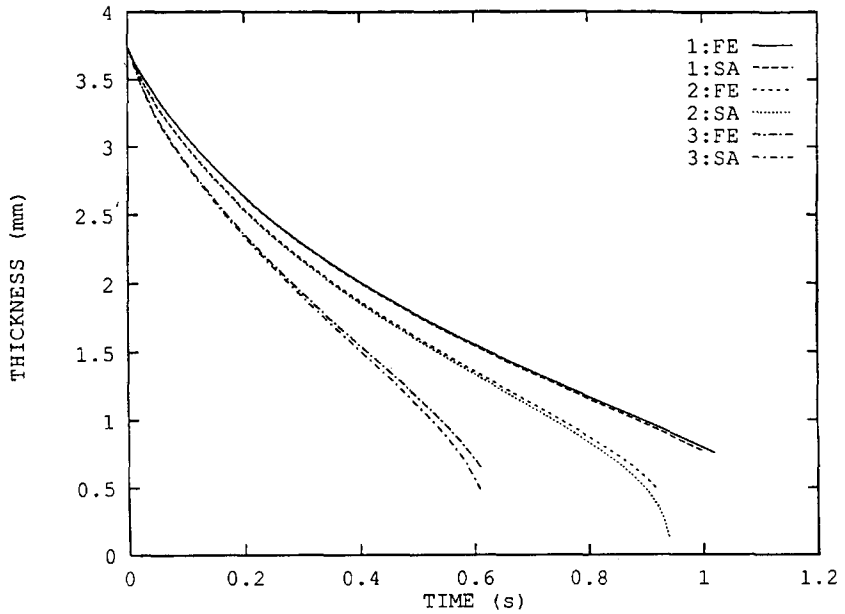

Fig. 7. Thickness of the tube vs. time.

The viscous elementary matrix $\boldsymbol{C}^{e}_{\eta_s}$ takes the following form:

$$\boldsymbol{C}^{e}_{\eta_s} = 2\eta_s \int_{\Omega^e_n} {}^{T}\mathrm{D}\boldsymbol{N} \cdot \mathrm{D}\boldsymbol{N}\, \mathrm{d}v^e, \tag{31}$$

where $\mathrm{D}\boldsymbol{N}$ expresses in vectorial form the strain rate tensor in terms of nodal velocities.

The bounded set of linear algebraic equations (20) is solved by a direct Crout decomposition.

3.6. Time step control associated with tool contact monitoring

The geometry of the tools (stretch rod and mold) is defined by a piecewise linear approximation. At time step t_n, the velocity field $\dot{u}_n$ allows one to determine the future trajectory of each node. One can then compute the intersection of each trajectory with the tools. The smallest of these intersection times is then retained as the value to be used for the next time step Δt_{n+1}.

3.7. Automatic remeshing

With an updated Lagrangian formulation, the nodes of the mesh following the kinematic evolution of the material points. This method may result in excessively distorted elements, when large deformations occur. An automatic remeshing procedure is used [16]. For each time interval, the procedure consists in the following steps:

(a) Check the distortion of the elements and the accuracy of the mesh boundary (penetration of the boundary nodes into the tools, curvature of boundary edges, . . .) in order to decide if remeshing must be started according to prescribed tolerances;

(b) addition of nodes on the current boundary (overdiscretization) and elimination of some of these nodes in order to generate an appropriate set of boundary nodes which must be compatible with the old mesh boundary and satisfy non-penetration conditions and the curvature condition;

(c) triangulation using Delaunay's algorithm [17] with addition of internal nodes in order to get triangle elements with the best possible shape;

(d) improvement of the shape of the elements by changing the diagonal of two adjacent neighboring triangles, and regularization of the mesh by moving the internal nodes toward the barycenter of adjacent nodes;

(e) numerical interpolation of the variables (especially stress variables) from the old mesh Ω_t to the new one Ω'_t.

As regards this last step of the procedure, the global least squares method is employed in order to minimize the quadratic error function between the unknown variable Λ' at new nodes of the domain Ω'_t and the known variable Λ at old nodes of the domain Ω_t (see Fig. 5).

Thus, we have

$$\underset{\forall \Lambda'}{\text{Min}} \left(\sum_{e=1}^{N_e} \int_{\Omega'_e} (\Lambda' - \Lambda)^2 \, \mathrm{d}v'_e \right)_{e = \text{element}} . \tag{32}$$

4. Applications

4.1. Validation test

The simultaneous inflation and stretching of a tube limited by two planes has been considered (Fig. 6). There is a perfectly sliding contact between the tube and the two planes which means that the part will always remain a tube. A constant elongation velocity v_0 is prescribed on the lower plane and the upper one has no displacement in the vertical direction. A differential inflation pressure ΔP is applied to the inner surface of the tube. A quasi-analytical model may be considered. Its results will be compared to the numerical model.

The rate of strain tensor as well as stress tensor are diagonal at each time step.

One can take advantage of the axisymmetric tube growth and use the Lagrangian coordinate transformation $(r, z) \rightarrow (X, Z)$:

$$X = \pi(r^2 - R^2)L = \pi(r'^2 - R'^2)L',$$

$$Z = \frac{z}{L} = \frac{z'}{L'}, \tag{33}$$

where (r, z, R, L) and (r', z', R', L') are respectively the radial coordinate, the axial coordinate, the inner radius and the length of the tube at time t and t'. Consequently, we have

$$\forall t \geq t' \geq 0 \qquad r = \sqrt{(r'^2 - R'^2)\frac{L'}{L} + R^2}, \quad z = z'\frac{L}{L'} \tag{34}$$

$$\forall t \leq 0 \qquad r = r_0 \qquad R = R_0 \qquad L = L_0. \tag{35}$$

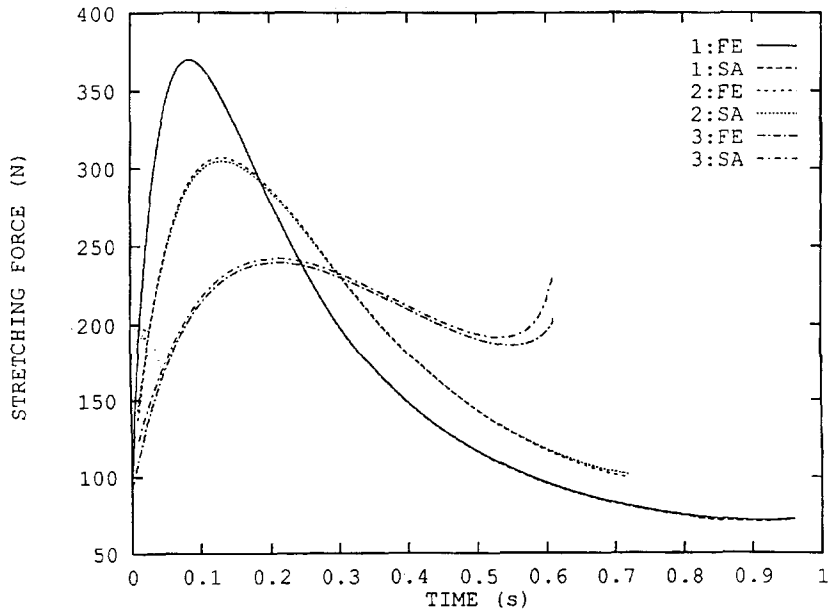

Fig. 8. Stretching force of the tube vs. time.

The orthoradial coordinates remain constant. The components of the extra-stress tensor can be more easily determined via the integral form of the Johnson–Segalman constitutive model which reduces in the case of an elongational flow to

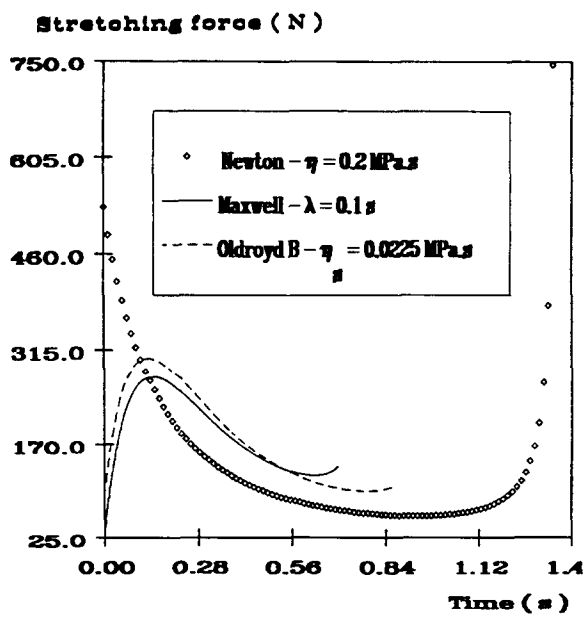

Fig. 9. Stretching force of the tube vs. time.

$$\boldsymbol{T} = \frac{1}{a}\int_{-\infty}^{t} m(t-t')\boldsymbol{C}^{-a}(t')\,\mathrm{d}t' \qquad (\forall a \neq 0), \tag{36}$$

where $\boldsymbol{C}^{-a}(t')|_{a=1}$ is the Finger strain tensor, $m(s)$ is the so-called memory function defined as

$$\forall s \geq 0 \qquad m(s) = \frac{\eta_v}{\lambda^2}\,\mathrm{e}^{-s/\lambda}.$$

The components of $\boldsymbol{C}^{-1}(t')$ are deduced from Eq. (34) (see Chung and Stevenson [18]). Dimensionless variables are introduced:

$$\tilde{\boldsymbol{T}} = \lambda\frac{\boldsymbol{T}}{\eta_v}, \qquad \tilde{t} = \frac{t}{\lambda}, \qquad \tilde{L} = \frac{L}{L_0}, \qquad \tilde{R} = \frac{R}{R_0}, \qquad \tilde{X} = \frac{X}{\pi L_0 R_0^2}, \qquad \tilde{\vartheta} = \frac{\vartheta}{\pi L_0 R_0^2} = \left(\frac{S_0}{R_0}\right)^2 - 1.$$

$\tilde{\vartheta}$ is the dimensionless volume of the circular tube. The dimensionless components of $\tilde{\boldsymbol{T}}$ are

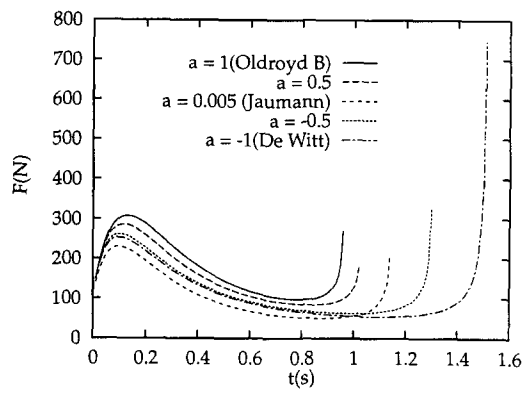

Fig. 10. Influence of the slip parameter on the stretching force.

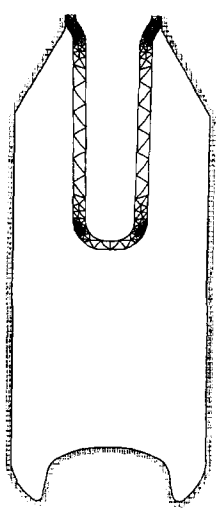

Fig. 11. Geometry of the bottle mold and initial preform mesh.

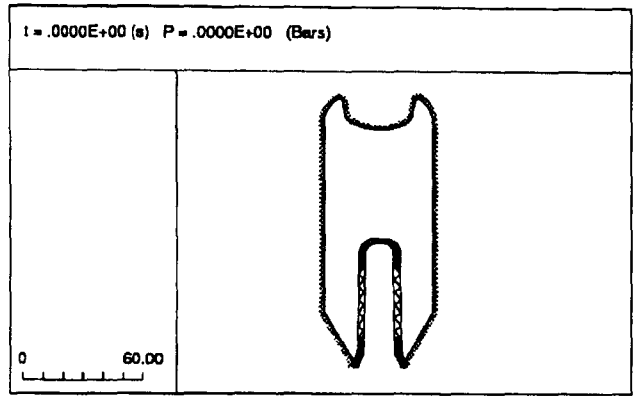
t = .0000E+00 (s) P = .0000E+00 (Bars)
0
60.00

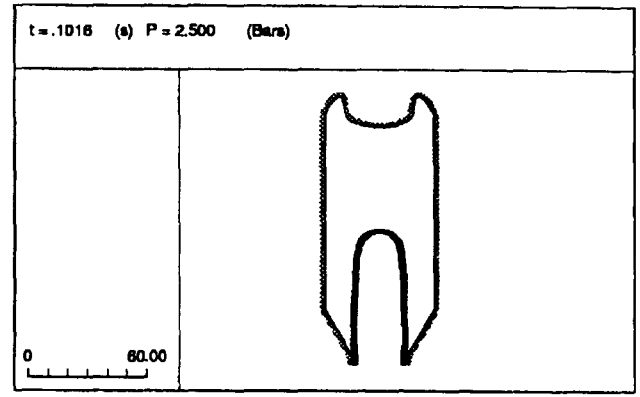
t = .1016 (s) P = 2.500 (Bars)
0
60.00

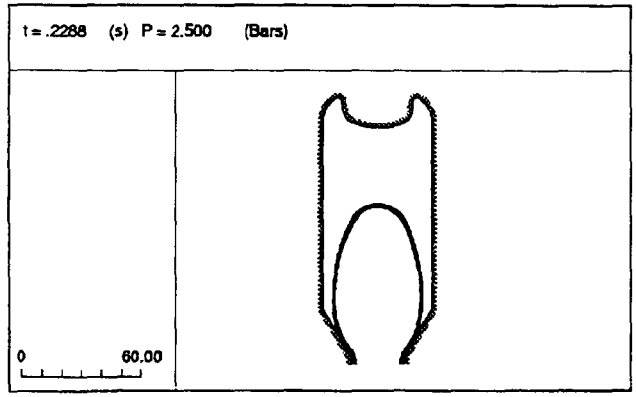
t = .2288 (s) P = 2.500 (Bars)
0
60.00

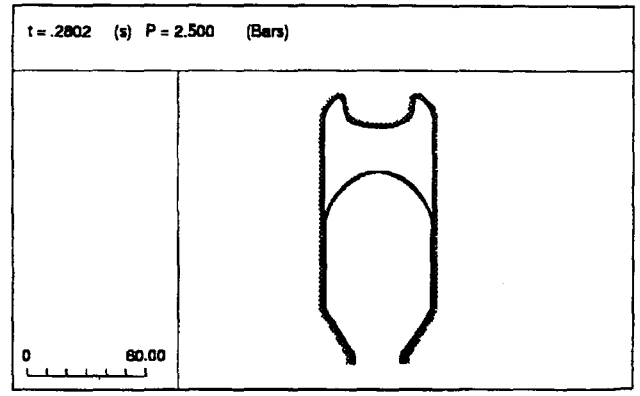
t = .2802 (s) P = 2.500 (Bars)
0
60.00

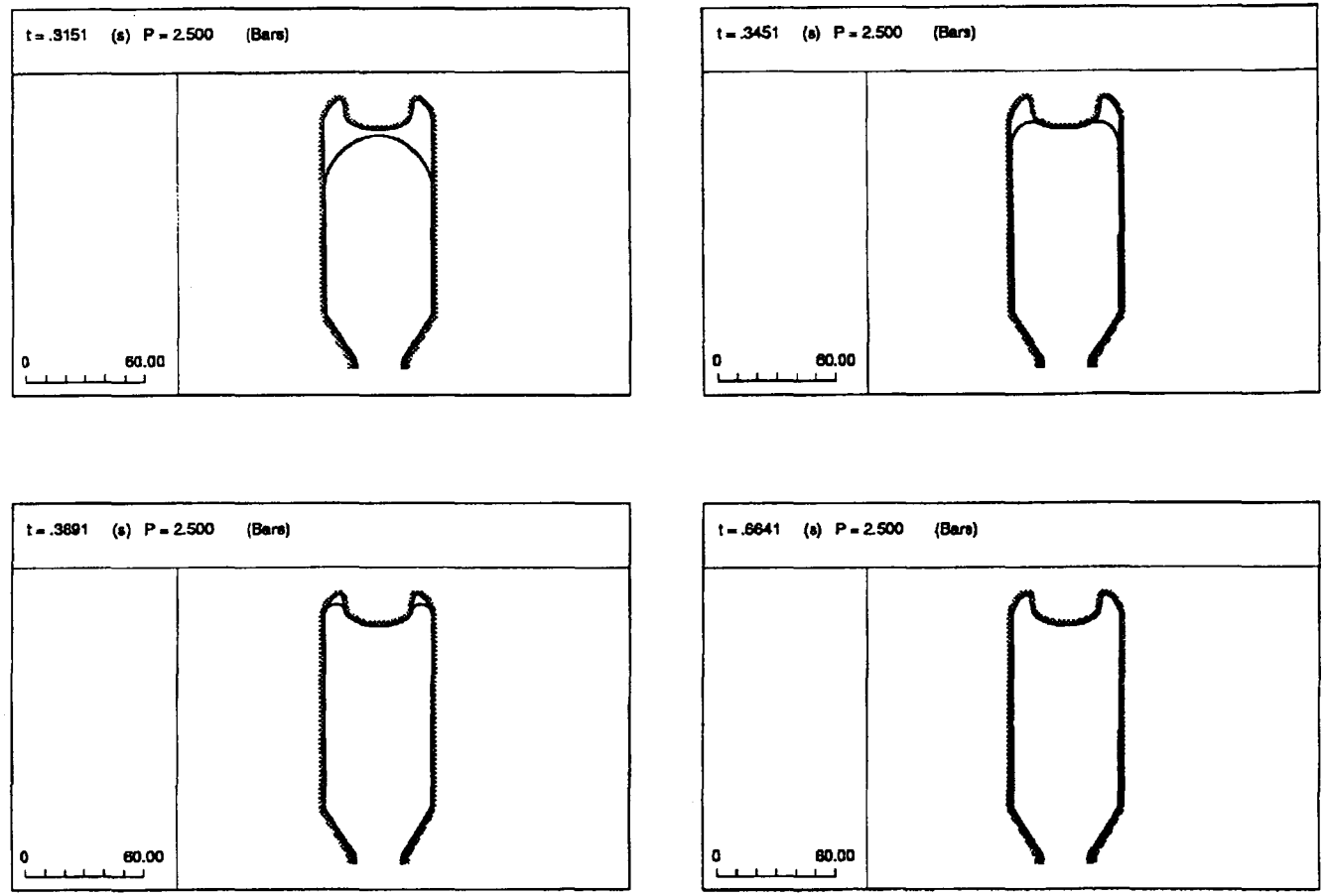

Fig. 12. Intermediate bottle shapes.

Table 2
Rheological parameters for the blow molding process

a	η_s (Pa · s)	λ (s)	η_v (Pa · s)
1.0	43×10^3	0.7	35×10^4

$$\tilde{T}_{rr} = \frac{e^{-\tilde{t}}}{a[\tilde{L}(\tilde{X} + \tilde{L}\tilde{R}^2)]^a} \left\{ (\tilde{X}+1)^a + \int_0^{\tilde{t}} e^{\tilde{t}} [\tilde{L}'(\tilde{X} + \tilde{L}'\tilde{R}'^2)]^a \, d\tilde{t}' \right\}, \tag{37}$$

$$\tilde{T}_{\theta\theta} = \frac{e^{-\tilde{t}}(\tilde{X} + \tilde{L}\tilde{R}^2)^a}{a\tilde{L}^a} \left\{ (\tilde{X}+1)^{-a} + \int_0^{\tilde{t}} e^{\tilde{t}} \left[\frac{\tilde{L}'}{(\tilde{X} + \tilde{L}'\tilde{R}'^2)} \right]^a d\tilde{t}' \right\}, \tag{38}$$

$$\tilde{T}_{zz} = \frac{\tilde{L}^{2a}}{a} e^{-\tilde{t}} \left(1 + \int_0^{\tilde{t}} \frac{e^{\tilde{t}} \, d\tilde{t}'}{\tilde{L}'^{2a}} \right). \tag{39}$$

Using the boundary condition given in Section 2, the integrated stress balance equation in the r-direction is

$$\Delta P + \int_R^S \frac{\sigma_{rr} - \sigma_{\theta\theta}}{r} \, dr = \int_R^S \rho \gamma_r \, dr. \tag{40}$$

Using the previous dimensionless variables, this gives

$$De + \left(\frac{\eta_s}{\eta_v} \right) \frac{\partial}{\partial t} \left[\ln \left(\frac{\tilde{\vartheta}}{\tilde{L}\tilde{R}^2} + 1 \right) \right] + \tfrac{1}{2} \int_0^{\tilde{\vartheta}} \frac{\tilde{T}_{rr} - \tilde{T}_{\theta\theta}}{\tilde{X}' + \tilde{L}\tilde{R}^2} \, d\tilde{X}' = Re \int_0^{\tilde{\vartheta}} \frac{\tilde{\gamma}_r}{2\tilde{L}\tilde{r}} \, d\tilde{X}', \tag{41}$$

where Re is the Reynolds number and De the Deborah number which are defined as:

$$De = \lambda \frac{\Delta P}{\eta_v}, \qquad Re = \frac{\rho R_0^2}{\lambda v_v}. \tag{42}$$

The nonlinear form of Eq. (41) precludes any simple analytical solution for $\tilde{R}$ except for some limiting cases, for example, when inertia effects are strongly dominant [19] ($Re \gg 1$) or for a Newtonian tube with inertia terms neglected ($Re \ll 1$). Classical values for the rheology of PET and for the blow molding parameters [20] (see Table 1) lead to the following characteristic values for Reynolds and Deborah numbers:

$$Re = 6 \times 10^{-4}, \qquad De = 0.5.$$

This indicates that the contribution of inertia effects will be much smaller than viscous and elastic effects.

At each time step, the dimensionless radius $\tilde{R}$ is determined from Eq. (41), using a quasi-Newton iterative procedure. The iterative scheme was stopped when successive values of $\tilde{R}$ differed by less than $10^{-3}\%$. Simpson's first rule was used to evaluate the integrals. Then, the components of the stress tensor and the stretching force are deduced.

The first calculation has been achieved using a constitutive equation of Oldroyd B type

($a = 1$ in Eq. (5)]. Three different relaxation times have been considered: $\lambda = 0.05$ s (no. 1), $\lambda = 0.1$ s (no. 2), and $\lambda = 0.2$ s (no. 3).

Figs. 7 and 8 show the comparison between the finite element calculation (FE) and the semi-analytic solution (SA) for the thickness and the stretching force vs. time (i.e. the force exerted on the moving plane which is related to the stress in the z-direction). The agreement is fair. The curve for the stretching force starts from zero, then reaches a maximum and decreases continuously. We note that when the relaxation time increases, the thickness of the tube decreases more rapidly and the initial slope of the stretching force decreases.

Fig. 9 compares the stretching force as a function of time for two viscoelastic constitutive equations (upper-convected Maxwell, Oldroyd B) and a Newtonian fluid with a viscosity $\eta_N = \eta_s + \eta_v$. The difference between the curves clearly indicates that a purely viscous model does not represent the increasing part of the curve which is directly related to the elastic response of the material.

Fig. 10 compares the stretching force as a function of time for different values of the slip parameter a ($a = -1, -0.5, 0.005, +0.5, +1$) and for $\lambda = 0.1$ s. We notice that the shape of the curves remains identical. The blowing time decreases as the slip parameter increases from -1 to $+1$.

4.2. Set up of real stretch/blow molding examples

Once the numerical model has been validated by comparing with a semi-analytic solution, we now investigate some more realistic cases. First, we present a blow molding process (no stretch rod). The geometry of the preform and the bottle has been furnished by Professor R.J. Crawford from the Queen's University of Belfast [20]. A constant internal pressure ΔP of 2.5×10^5 Pa is

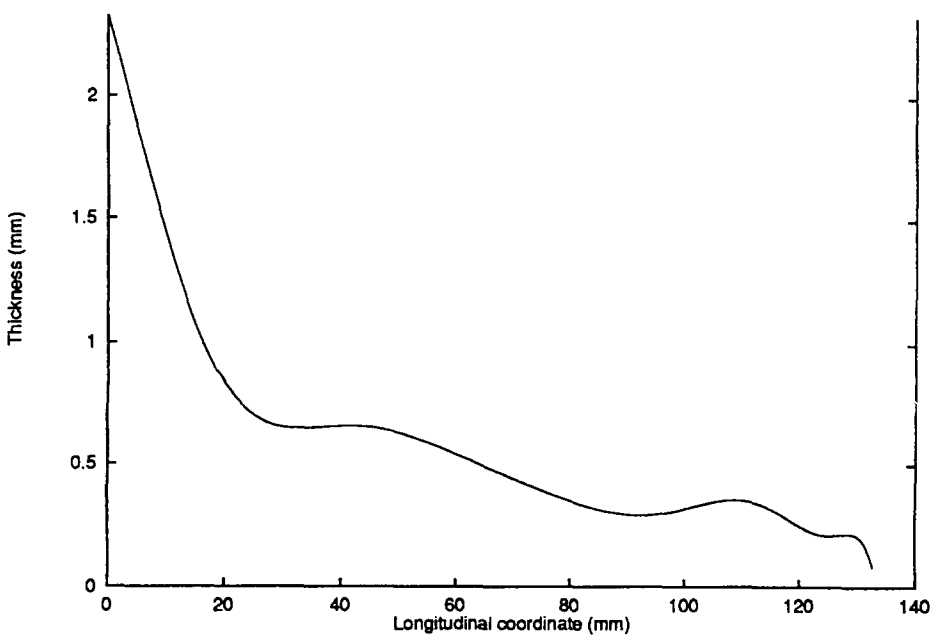

Fig. 13. Thickness distribution of the bottle.

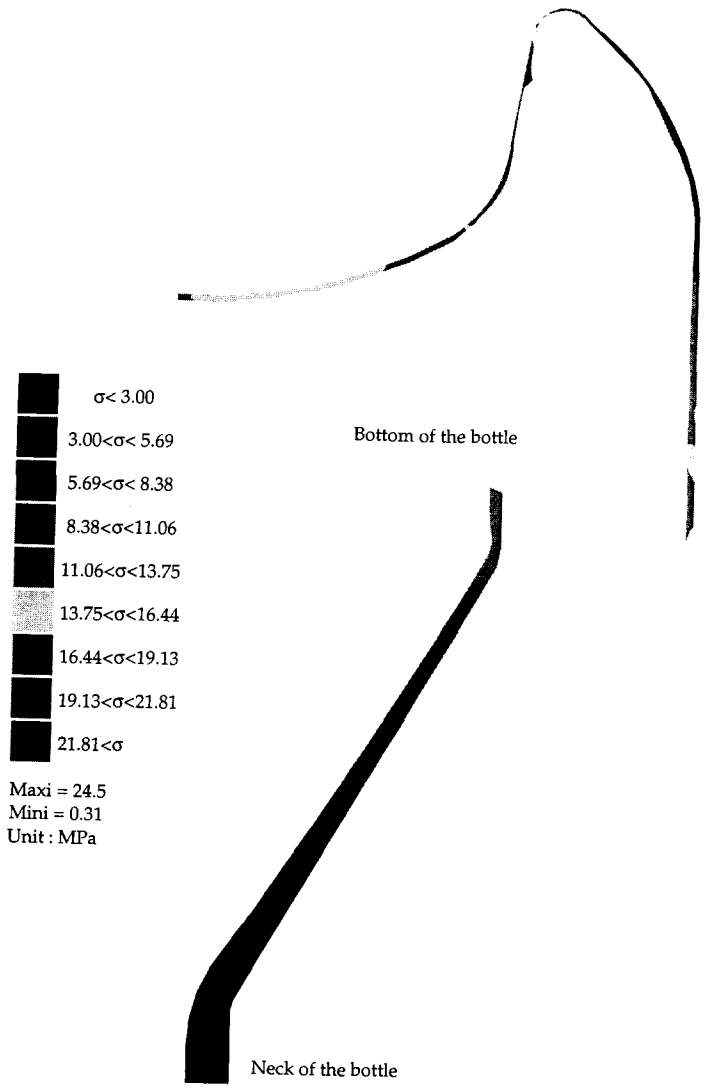

Fig. 14. Generalized stress distribution at the end of the process.

prescribed. The rheological parameters of the PET are given in Table 2. They have been determined by fitting to the traction force on an amorphous PET sample, injected under the same conditions as the tube shaped preform.

Fig. 11 shows the geometry of the bottle mold and the initial mesh of the preform. Fig. 12 presents intermediate bottle shapes from the beginning of the process to the end. Fig. 13 presents the thickness distribution vs. longitudinal coordinate at the end of the process.

A zoom of the neck and the bottom of the bottle (Fig. 14) shows the stress distribution at the end of the process. In cleary indicates that at the end of the process, the bottom of the bottle is submitted to high stresses.

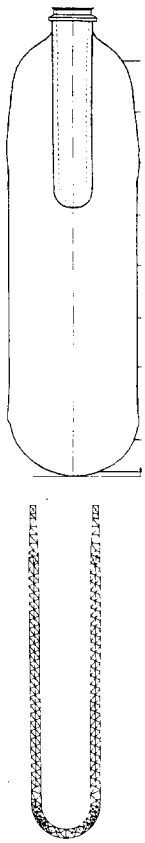

Fig. 15. Geometry of the bottle mold and initial preform mesh.

We study now a stretch/blow molding operation. Fig. 15 shows the geometry of the bottle mold and the initial mesh of the preform. The dimensions of the bottle mold and the preform are given in Table 3. The rheological parameters are the same as those given in Table 2. The process parameters are given in Table 4. The prescribed pressure is a time-dependent function (i.e. stretch/blow using preblow and blow).

v_0 is the velocity of the stretch rod which is applied as long as the preform contacts the bottom of the mold, P_{ps} is the maximum pre-blowing pressure (low pressure) imposed during $t \in [0, t_{ps}]$, and P_s the maximum blowing pressure (high pressure) imposed during $t \in [t_{ps}, t_{ps} + t_s]$.

Table 3
Dimensions of the bottle mold and the preform

Material	Length (mm)	Inner radius (mm)	External radius (mm)
Preform	125	9.275	13.025
Bottle mold	310	44.3	44.3

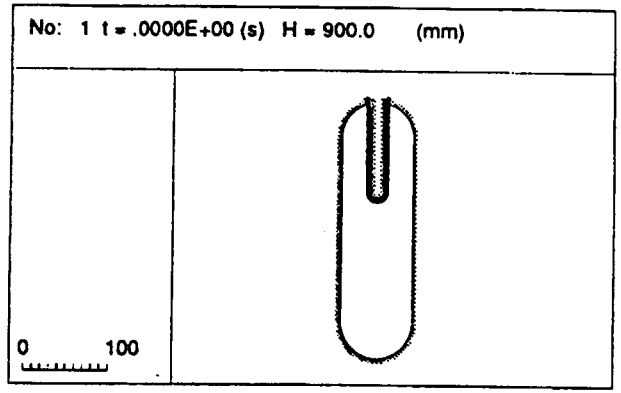
No: 1 t = .0000E+00 (s) H = 900.0 (mm)
0
100

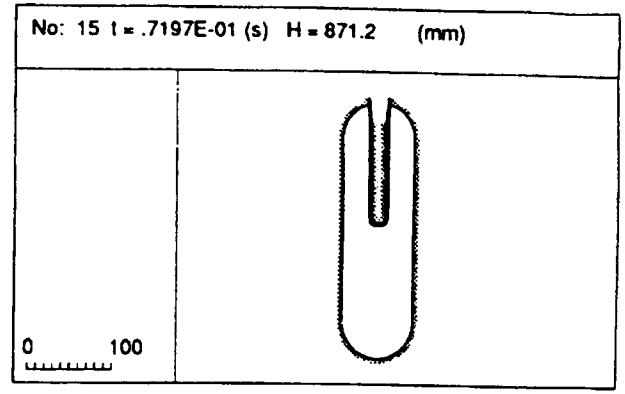
No: 15 t = .7197E-01 (s) H = 871.2 (mm)
0
100

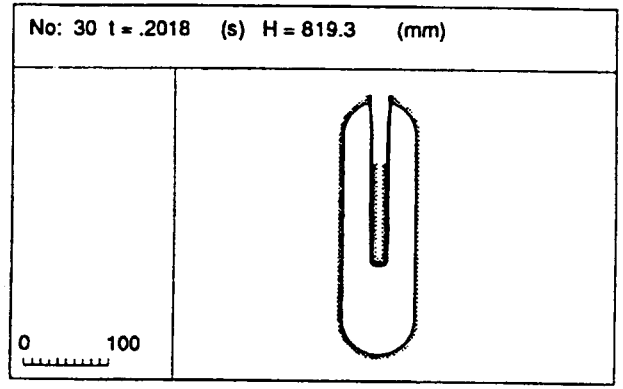
No: 30 t = .2018 (s) H = 819.3 (mm)
0
100

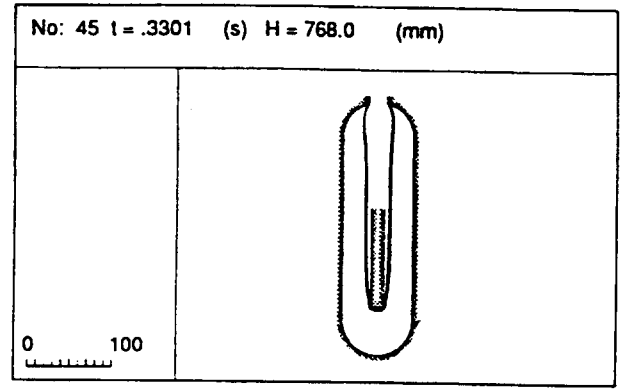
No: 45 t = .3301 (s) H = 768.0 (mm)
0
100

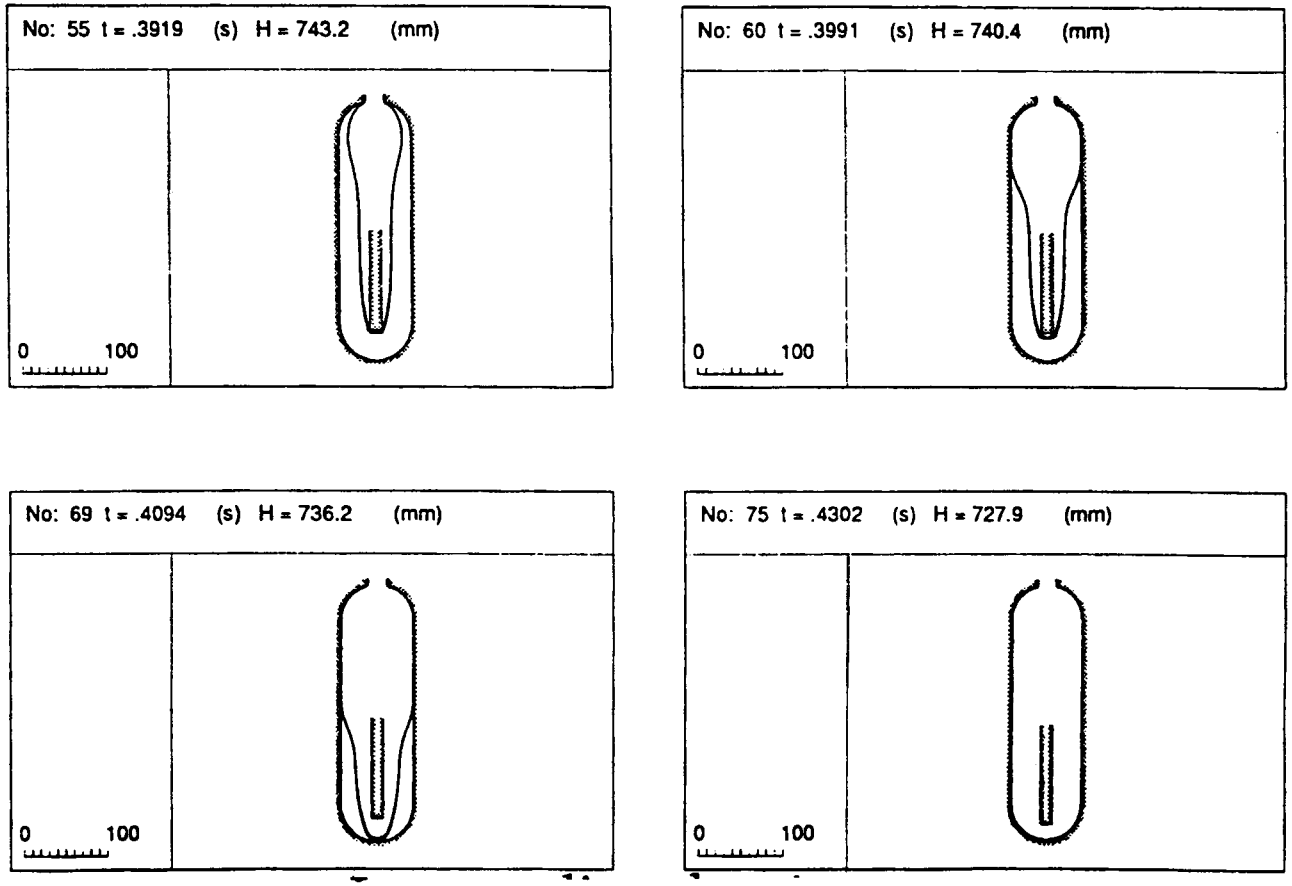

Fig. 16. Intermediate bottle shapes.

Table 4
Rheological parameters for the stretch/blow molding process

v_0 (m s^{-1})	P_{ps} (Pa)	t_{ps} (s)	P_s (Pa)	t_s (s)
0.4	8×10^5	0.2	20×10^5	0.8

Fig. 16 presents intermediate bottle shapes from the beginning of the process to the end.

Comparisons with experimental measurements have been done. The measured and computed stretching forces on the stretch rod vs. time are plotted in Fig. 17 for two velocities of the stretch rod; 0.2 and 0.4 m s^{-1}.

We note that there is a qualitative agreement between computation and measurement: the stretching force starts from zero (or from a very low value), reaches a maximum and then decreases. A Newtonian analysis would lead to a continuously decreasing stretching force.

The comparison between the computed thickness and the experimental data is shown in Fig. 18. We note that even if the calculated and experimental results of stretching differ (Fig. 17), the agreement between the computed thickness and the experimental data is fair.

5. Conclusion

Successful numerical simulations of the stretch/blow as well as blow molding processes have

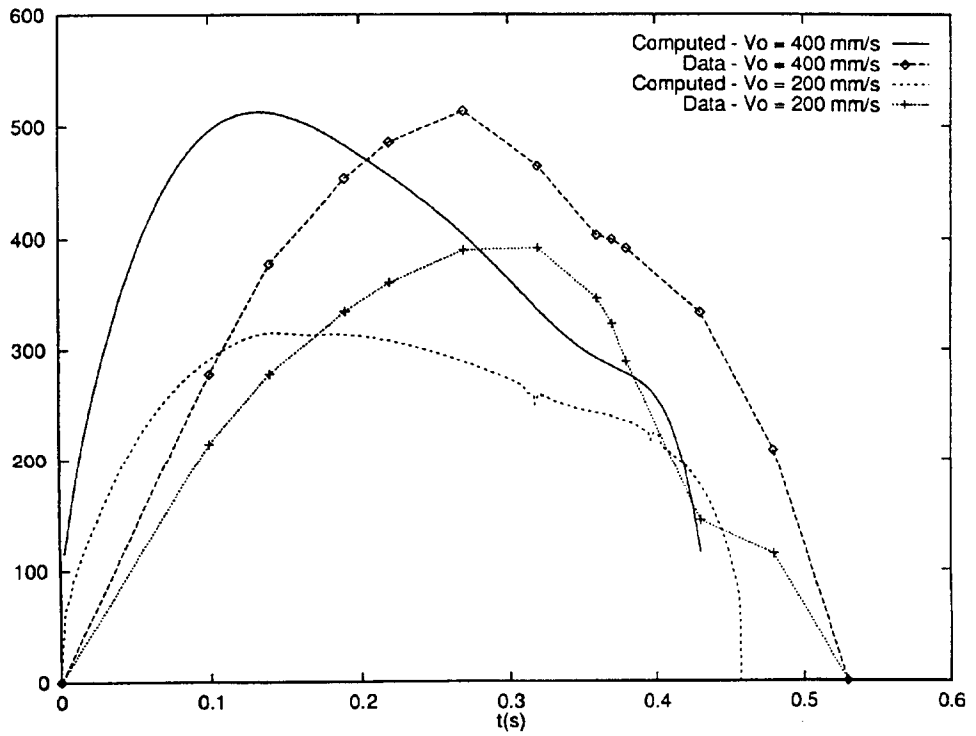

Fig. 17. Stretching force vs. time; effects of the plug velocity.

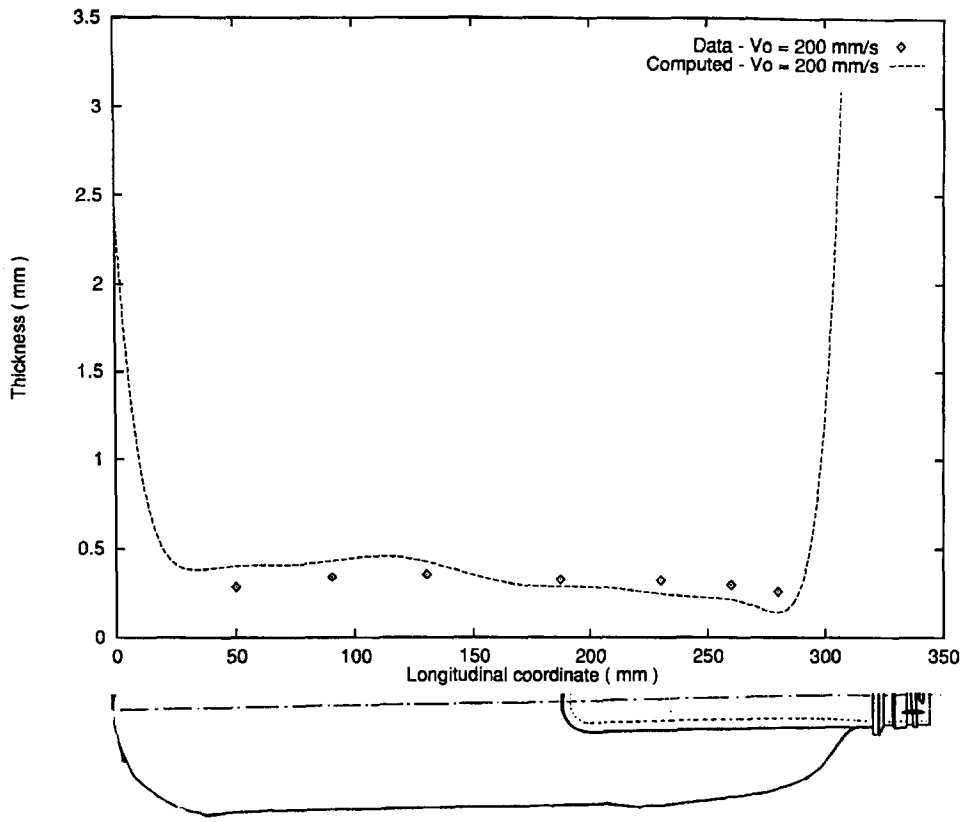

Fig. 18. Thickness distribution at the end of the process.

been performed using viscoelastic constitutive equations.

The volumic mechanical computations using the finite element method have allowed us to predict the thickness distribution, the contact kinetic and the stress distribution.

In the future, a coupled thermomechanical formulation should be developed in order to account for the temperature gradients that affect the preform during the process. A preliminary development has been carried out in that sense, taking into account the transient heat transfer in the preform [21]. However, this raises the problem of the identification of the constitutive equation parameters for PET at high strain rates and evolving temperature, and more generally, the problem of coupling between microstructural evolution and the thermomechanical history, which still remains an open issue.

Acknowledgments

This research was supported by the Sidel Company and the French Ministère de la recherche (MRT no. 90A 136).

References

[1] M.K. Warby and J.R. Whiteman, Finite element model of viscoelastic membrane deformation, Comput. Methods Appl. Mech. Eng., 68 (1988) 33–54.

[2] H.G. De Lorenzi, H.F. Nied and A. Taylor, Three-dimensional finite element thermoforming, Polym. Eng. Sci., 30 (20) 1990.

[3] H.G. De Lorenzi and H.F. Nied, Finite element simulation of thermoforming and blow molding, in A.I. Isayev (Ed.), Progress in Polymer Processing, Hanser Verlag, 1991.

[4] K. Kouba and J. Vlachopoulos, Modeling of thermoforming and blow molding, theoretical and applied rheology, Proceedings XIth Congress on Rheology, Brussels, Belgium, 17–21 August, 1992.

[5] J.M.A. Cesar de Sa, Numerical modelling of glass forming processes, Eng. Comput., 3, December 1986.

[6] K. Chung, Finite element simulation of PET stretch/blow-molding process, J. Mater. Shap. Tech., 7 (4) (1989) 229–239.

[7] A.J. Poslinski and J.A. Tsamopoulos, Nonisothermal parison inflation in blow molding, AIChE J., 36 (12) (1990).

[8] B. Debbaut, B. Hocq and J.M. Marchal, Numerical simulation of the blow moulding process, ANTEC '93, May 1993.

[9] F.M. Schmidt, J.F. Agassant, M. Bellet and G. Denis, Numerical simulation of polyester stretch/blow molding process, Numiform 92, Proceedings 4th International Conference on Numerical Methods in Industrial Forming Processes, Balkema, September 1992, pp. 383–388.

[10] M.W. Johnson and D. Segalman, A model for viscoelastic fluid behavior which allows non-affine deformation, J. Non-Newtonian Fluid Mech., 2 (1977) 255–270.

[11] M.J. Crochet, A.R. Davies and K. Walters, Rheology Series, Vol. 1, Numerical Simulation of Non-Newtonian Flow, Elsevier, Amsterdam, 1984, p. 199.

[12] N.M. Newmark, A method of computation of structural dynamics, ASCE J. Eng. Mech. Div., 85 (1959) 67–94.

[13] R. Keunings, Simulation of viscoelastic flow, in C.L. Tucker III (Ed.), Fundamentals of Computer Modeling for Polymer Processing, Hanser Publishers, 1989.

[14] F.G. Basombrio, Flow of viscoelastic fluids treated by the method of characteristics, J. Non-Newtonian Fluid Mech., 39 (1991) 17–54.

[15] P.T. Baaijens, Numerical analysis of unsteady viscoelastic flow, Comput. Methods Appl. Mech. Eng., 94 (1992) 285–299.

[16] T. Coupez, Grandes transformations et remaillage automatique, Thèse de Doctorat en Sciences et Génie des Matériaux, Ecole des Mines de Paris, 1991.

[17] D.F. Watson, Computing the n-dimensional Delaunay tessellation with application to Voronoï polytopes, Comput. J., 24 (2) (1981) 167–172.

[18] S.C. Chung and J.F. Stevenson, A general elongation experiment: inflation and extension of a viscoelastic tube, Rheol. Acta, 14 (1975) 832–841.

[19] R.E. Khayat and A. Garcia Rejon, Uniaxial and biaxial unsteady inflations of a viscoelastic material, J. Non-Newtonian Fluid Mech., 43 (1992) 31–59.

[20] McEvoy, C.G. Armstrong and R.J. Crawford, Simulation of the Stretch Blow Moulding Process of PET Bottles, UK ABAQUS User Group, 1994.

[21] F.M. Schmidt, J.F. Agassant, M. Bellet and L. Desoutter, Thermo mechanical simulation of PET Stretch/Blow molding process, PPS Annual meeting, Akzou (USA), 1994.